ROYAL SOCIETY
OF CHEMISTRY

PAPER

Check for updates

Integrating $ZnCo_2O_4$ submicro/nanospheres with Co_xSe_y nanosheets for the oxygen evolution reaction and zinc–air batteries†

Zequn Mai, [ID] [a] Wentao Duan, [b] Kai Wang, [ID] [a] Zhenghua Tang [ID] *[ac] and Shaowei Chen [ID] [d]

Developing low cost, high-efficiency and robust electrocatalysts to boost the oxygen evolution reaction (OER) is of great significance for clean energy storage and conversion devices such as electrochemical water splitting devices, rechargeable zinc–air batteries, and so on. In this study, we present a facile means to integrate $ZnCo_2O_4$ submicro/nanospheres with Co_xSe_y (x and y denote the molar ratio of Co and Se, respectively) nanosheets, and such a composite exhibited excellent OER activity with an overpotential of 324 mV at 10 mA cm^{-2} in 1 M KOH. It also exhibited superior long-term stability to the benchmark IrO_2 catalyst. In the home-made zinc–air battery test, the battery modified with the composite as the air cathode showed excellent performance with a small voltage gap of 0.98 V at 50 mA cm^{-2}, a high power density of 212.9 mW cm^{-2}, a high specific capacity of 570.1 mA h g^{-1}, and a stable cycling stability (50 h) at 10 mA cm^{-2} with a round-trip efficiency of 56.3%, superior to the IrO_2/C counterpart. This study can provide an avenue for developing cost effective, efficient and durable OER electrocatalysts as alternatives for various renewable energy storage and conversion devices.

Introduction

The fast-growing demand for clean energy has provoked intense research efforts for developing efficient, inexpensive energy storage and conversion devices. Electrochemical water splitting can provide a potential means for producing clean and renewable hydrogen fuels to power human civilization,[1–7] while rechargeable zinc–air batteries are attracting worldwide attention due to their merits of low cost, high theoretical energy density, and safe operation.[8–13] However, the high overpotential and sluggish reaction kinetics of the oxygen evolution reaction (OER) significantly impede the overall efficiency for the above devices.[14–18] In addition, an ideal OER catalyst should be

composed of nontoxic mechanically and chemically stable earth-abundant elements, and electrically conductive materials to be integrated in the electrodes.[19–21] To this end, enormous efforts have been devoted to developing various OER catalysts with high efficiency, low cost, and robust durability.[22–25] However, the oxides of iridium and ruthenium (IrO_2 and RuO_2) are still considered as the state-of-the-art catalysts for the OER,[26–29] but their high costs and extremely low earth reserves of the noble metals (Ru and Ir) as well as the insufficient long-term durability of such catalysts significantly limit their large scale deployment.[30,31] Hence, developing low cost, high-efficiency and durable OER catalysts that are at least comparable with, if not superior to, the IrO_2/RuO_2 benchmarks is imperative.[32–35]

Cobalt based OER catalysts including cobalt oxides,[36,37] cobalt phosphides,[38] cobalt sulfides,[39] cobalt selenides,[40] and other cobalt-containing composites[41,42] have been of recent intense interest mainly due to their desirable activity and stability in various electrolytes. In particular, because of the high conductivity of cobalt selenides compared with oxides, phosphides, and sulfides, cobalt selenides can achieve relatively superior OER performance.[40,43] For instance, Liu *et al.* developed $CoSe_2$ ultrathin nanosheets with atomic thickness, which could effectively catalyze the OER reaction with a low overpotential, small Tafel slope, and large turnover frequency.[44] The X-ray absorption fine structure analysis and first-principles calculations offered clear evidence that a number of vacancies were formed in the ultrathin $CoSe_2$ nanosheets, which served as active sites to effectively adsorb water molecules.[44] Liu and co-

[a]Guangzhou Key Laboratory for Surface Chemistry of Energy Materials, New Energy Research Institute, School of Environment and Energy, South China University of Technology, Guangzhou Higher Education Mega Centre, Guangzhou, 510006, P. R. China. E-mail: zhht@scut.edu.cn

[b]College of Chemical Engineering, North China University of Science and Technology, Tangshan, Hebei, 063009, China

[c]Guangdong Engineering and Technology Research Center for Surface Chemistry of Energy Materials, School of Environment and Energy, South China University of Technology, Guangzhou Higher Education Mega Centre, Guangzhou, 510006, P. R. China

[d]Department of Chemistry and Biochemistry, University of California, 1156 High Street, Santa Cruz, California 95064, USA

† Electronic supplementary information (ESI) available: The detailed calculation for turnover frequency and mass activity, additional tables, SEM images, XPS spectra, and cyclic voltammograms, and open-circuit voltage plots. See DOI: 10.1039/c9se01253b

workers documented the fabrication of new monoclinic Co_3Se_4 thin nanowires on cobalt foam, which delivered current densities of 10 and 20 mA cm^{-2} at low cell voltages of 1.59 and 1.63 V, respectively.[45] On the other hand, a previous study has shown that as one of the mixed valence oxides of Co, zinc cobaltite ($ZnCo_2O_4$) exhibited good OER performance with lower overpotential and Tafel slope values than those of crystalline oxides.[46] The composite of zinc cobaltite and cobalt selenide could achieve high performance of the OER, and a facile strategy to integrate both is highly desirable, and this is the primary goal of our current study.

Herein, we report a facile approach to integrate $ZnCo_2O_4$ submicro/nanospheres with Co_xSe_y nanosheets, and electronic microscopic measurements revealed that a 3D structure of $ZnCo_2O_4$ submicro/nanospheres with Co_xSe_y nanosheets (x and y denote the molar ratio of Co and Se, respectively) including both Co_9Se_8 and $CoSe$ was acquired. The $ZnCo_2O_4/Co_xSe_y$ composite exhibited excellent OER activity and remarkable long-term stability in alkaline media, superior to the benchmark IrO_2 catalyst. Besides, in the practical application of rechargeable zinc–air batteries, the battery modified with the $ZnCo_2O_4/Co_xSe_y$ composite as the air cathode demonstrated intriguing performance as well, outperforming the IrO_2/C decorated battery.

Experimental section

Reagents and materials

Zinc nitrate hexahydrate ($Zn(NO_3)_2 \cdot 6H_2O$, ≥99.0%) was obtained from Guangzhou Chemical Reagent Factory, Guangzhou, China. Sodium acetate anhydrous (NaOAc, 99.0%) and ethanol (≥99.7%) were purchased from Damao Chemical Reagent, Tianjin, China. Cobalt acetate tetrahydrate ($Co(OAc)_2 \cdot 4H_2O$, ≥99.5%) was bought from Kermel Chemical Reagent, Tianjin, China. Selenium dioxide (SeO_2, 99.0%), iridium dioxide (IrO_2, 99.9%), cobaltous nitrate hexahydrate ($Co(NO_3)_2 \cdot 6H_2O$, 99.99%), poly(ethylene glycol) (PEG-200, MW = 200) and benzyl alcohol (99.9%) were purchased from Energy Chemicals, Shanghai, China. 5 wt% Nafion solution used in the electrochemical measurements was produced by Du Pont Company, USA. Deionized water with a resistivity of 18.2 MΩ cm^{-1} was used in this work. All chemicals were received from commercial sources and used without further purification.

The preparation of $ZnCo_2O_4$

In a typical synthesis, 5 mmol $Zn(NO_3)_2 \cdot 6H_2O$, 10 mmol $Co(NO_3)_2 \cdot 6H_2O$ and 30 mmol NaOAc were co-dissolved in 20 mL PEG-200 forming a transparent solution. After stirring for over 1 h, the solution was transferred into a 100 mL Teflon-lined stainless-steel autoclave and maintained at 200 °C for 32 h. Followed by cooling down to room temperature naturally, the resulting precipitates were collected by centrifugation and washed with ethanol at least three times and dried in a vacuum oven at 35 °C for about 20 h. Finally, the precursor powder was annealed under an air atmosphere at 300 °C for 2 h at a heating rate of 1 °C min^{-1} to obtain $ZnCo_2O_4$.

The preparation of Co_xSe_y and $ZnCo_2O_4/Co_xSe_y$

The synthesis of $ZnCo_2O_4/Co_xSe_y$ was realized by a facile solvothermal method using the as-prepared $ZnCo_2O_4$ as a template. Specifically, 15 mg $ZnCo_2O_4$ was first dispersed in 23 mL benzyl alcohol, followed by sonication for 20 min to obtain a homogeneous solution. Then, $Co(OAc)_2 \cdot 4H_2O$ and SeO_2 with a molar ratio of 1 : 1 were sequentially added into the above solution under vigorous magnetic stirring. After ∼80 min, the dark-purple solution was transferred into a 50 mL Teflon-lined stainless-steel autoclave and heated at 180 °C for 6 h followed by naturally cooling down to room temperature. After centrifugation at a speed of 10 000 rpm for 2 min, the formed black precipitates were washed with ethanol several times, and the product of $ZnCo_2O_4/Co_xSe_y$ was dried at 35 °C in a vacuum for one day. For comparison, Co_xSe_y was also prepared in the same manner without adding $ZnCo_2O_4$.

Characterization

The crystal structure information on the catalysts was recorded by X-ray powder diffraction with a Bruker D8-Advance diffractometer using Cu K$_\alpha$ radiation ($\lambda = 0.1541$ nm). The chemical composition and the valence states of the elements in the samples were analyzed by X-ray photoelectron spectroscopy (XPS) measurements with an Escalab 250 photoelectron spectrometer (Thermo Fisher Scientific, USA). The morphologies and surface structures were observed by field-emission scanning electron microscopy (FE-SEM, Hitachi S-4800) and transmission electron microscopy (TEM, JEOL JEM-2100F). High-resolution transmission electron microscopy (HR-TEM), and energy dispersive X-ray spectroscopic (EDS) elemental mapping were performed on a FEI Tecnai F20 machine.

Electrochemical measurements

The OER measurements were performed on a CHI 750E electrochemical workstation (CH Instruments Inc.) in a 1 M KOH aqueous solution at room temperature coupled with a conventional three-electrode system. Platinum foil and an Ag/AgCl electrode were used as the counter and reference electrodes, respectively. The as-prepared catalyst loaded on a glassy carbon electrode (GCE, diameter of 5 mm) was employed as the working electrode, which was prepared as follows. 5 mg of the as-prepared catalyst or IrO_2 was first dispersed in 1 mL ethanol with 20 μL 5 wt% Nafion solution by sonicating for 30 min to form a homogeneous ink. Then, 40 μL of the catalyst ink was drop-cast onto the surface of the GCE and left to be dried naturally at room temperature with a catalyst mass loading of ∼1.02 mg cm^{-2}. The polarization curves were recorded from 0 to 1.0 V at a scan rate of 10 mV s^{-1} with a rotation speed of 1600 rpm without iR correction. The Tafel slope was calculated according to the Tafel equation as follows: $\eta = b \times \log(j/j_0)$, where η denotes the overpotential, b is the Tafel slope, j represents the current density, and j_0 represents the exchange current density. The electrochemical impedance spectroscopic (EIS) measurements were carried out at an overpotential of 343 mV from the frequency range of 100 kHz to 0.01 Hz. The

long-time stability test was obtained after repeated scans from 0 to 0.5 V with a sweep rate of 50 mV s^{-1}. Multistep chronopotentiometric measurements were performed with varying current densities starting from 20 mA cm^{-2} to 200 mA cm^{-2}, with an increment of 20 mV cm^{-2} per 500 s without *iR* correction. Accelerated durability tests (ADTs) of the samples were measured with the potential cycled in a 1 M KOH solution between 0 and 0.5 V at the scan rate of 100 mV s^{-1}.

The electrochemically active surface area (EASA) values of the catalysts were determined according to the reported method.[20,45] The electrochemical double-layer capacitance (C_{dl}) was estimated by cyclic voltammetric curves collected in the non-faradaic region of 0.9–1.03 V *vs.* RHE at the scan rate of 10, 20, 30, 40, and 50 mV s^{-1}, respectively. Turnover frequency (TOF) and mass activity (MA) values of the catalysts were calculated by following the equations in previous reports (see details in the ESI†).[43,47] The ORR test was also performed under the same conditions but in an O$_2$-saturated 0.1 M KOH solution with a catalyst mass loading of 0.255 mg cm^{-2}. The LSV measurements were performed in the potential range from −0.033 V to +1.166 V (*vs.* RHE) with a scan rate of 10 mV s^{-1} at a rotation speed of 1600 rpm. All potentials are reported *versus* the reversible hydrogen electrode (RHE) by converting the potentials measured *vs.* Ag/AgCl according to the following equation: $E_{RHE} = E_{Ag/AgCl} + 0.197 + 0.0591 \times pH$.

Rechargeable zinc–air battery performance measurement

The rechargeable zinc–air battery was constructed with a self-assembled zinc–air cell by using a Zn plate as the anode, hydrophobic carbon cloth with the catalyst loading on the water-facing side as the air-cathode and the air-facing side as the gas diffusion layer, and 6 M KOH solution containing 0.2 M Zn(OAc)$_2$·2H$_2$O as the electrolyte. For the preparation of the catalyst ink, 4 mg of the as-prepared sample was dispersed in 800 μL Nafion solution (0.5 wt%) by ultrasonic treatment for 30 min. Then, the above ink was drop-cast onto the hydrophobic side of carbon cloth with a catalyst loading of 4 mg cm^{-2}. For the preparation of the IrO$_2$/C catalyst (wt% of IrO$_2$ is 20%), 3.2 mg carbon black and 0.8 mg IrO$_2$ were mixed and dispersed in 800 μL Nafion solution (0.5 wt%). After 30 min ultrasonic processing, the above mixed dispersion was employed for the control test. The zinc–air battery test was performed using a LAND CT2001A battery program-control test system. The discharge and charge polarization curves were tested using a CHI440 electrochemical work station. The detailed calculations of the performance parameters can be found in the ESI.†

Results and discussion

The ZnCo$_2$O$_4$/Co$_x$Se$_y$ composite is synthesized by a two-step solvothermal method, as illustrated in Scheme 1. The ZnCo$_2$O$_4$ submicro/nanospheres are prepared by a solvothermal treatment in the presence of Co and Zn salt solution and a subsequent calcination in air at 300 °C for 2 h. Then, the ZnCo$_2$O$_4$ submicro/nanospheres are used as the template to
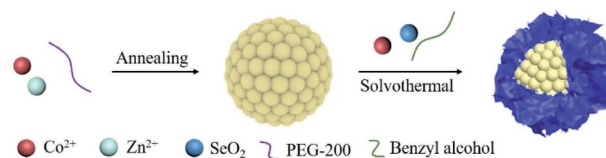
Scheme 1 The schematic for preparing the ZnCo$_2$O$_4$/Co$_x$Se$_y$ composite.

grow Co$_x$Se$_y$ on the surface by a further solvothermal method with SeO$_2$ as the Se source in benzyl alcohol.

Fig. S1† illustrates the typical SEM image of the ZnCo$_2$O$_4$ hierarchical structure, where uniform microspheres assembled with plenty of one-dimensional nanoparticles intercrossing with each other can be readily recognized. Fig. 1a and b show the representative SEM images of ZnCo$_2$O$_4$/Co$_x$Se$_y$, where spherical particles with numerous sheets on the surface can be easily identified in the dimension of ∼200–300 nm. The typical TEM images in Fig. 1c and d reveal that a single sphere contains a solid core inside and numerous interstacked sheets outside onto the core surface. The further high-resolution (HR) TEM image of the core in Fig. 1e demonstrates that a lattice fringe of 0.284 nm can be attributed to the crystal plane of (220)[48] from the spinel-phased ZnCo$_2$O$_4$. Moreover, the high-resolution (HR) TEM image in Fig. 1f shows well-defined crystal phases, and an interplanar spacing of 0.264 nm corresponds to the (002) crystal plane of CoSe,[49] while an interplanar spacing of 0.201 nm can be attributed to the (511) plane of Co$_9$Se$_8$.[50] This suggests the coexistence of both Co$_9$Se$_8$ and CoSe, and ZnCo$_2$O$_4$/Co$_x$Se$_y$ possessed a composite structure comprising ZnCo$_2$O$_4$ submicro/nanospheres and mixed CoSe/Co$_9$Se$_8$ nanosheets. The composite architecture of ZnCo$_2$O$_4$/Co$_x$Se$_y$ was further attested by the elemental mappings. As illustrated in Fig. 1g–k, the dark-field TEM image and elemental mapping images indicate the homogeneous distribution of Co, O, Zn, and Se throughout the composite.
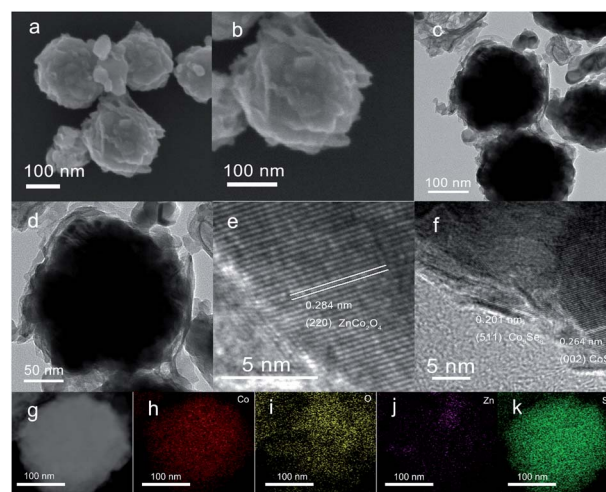

Fig. 1 (a) and (b) Representative SEM images, (c−f) the corresponding TEM and HR-TEM images with different magnifications, (g) dark field-TEM image, and (h−k) elemental mapping of ZnCo$_2$O$_4$/Co$_x$Se$_y$.

The crystal structure of $ZnCo_2O_4/Co_xSe_y$ was further verified by the XRD test. As illustrated at the bottom of Fig. 2a, the Bragg reflections at 31.4°, 36.9°, 38.6°, 44.9°, 55.9°, 59.4°, and 65.4° are in good accordance with the reported (220), (311), (222), (400), (422), (511) and (440) crystal phases of the $ZnCo_2O_4$ spinel structure (JCPDS No. 23-1390).[51] For Co_xSe_y in the top of Fig. 2a, the 2θ peaks positioned at 33.5°, 45.2°, and 50.9° are from hexagonal CoSe (JCPDS No. 23-1390), while the other peaks at 28.4°, 29.9°, 45.2°, 49.6°, and 58.6° are assigned to cubic Co_9Se_8 (JCPDS No. 09-0233).[52] The right panel in Fig. 2b shows the XRD patterns of $ZnCo_2O_4/Co_xSe_y$. One can clearly see that the XRD profile features all three species with slight shifts, further confirming that the composite of $ZnCo_2O_4$ integrated with both CoSe and Co_9Se_8 was successfully obtained.

Subsequently, the chemical composition and charge states of the $ZnCo_2O_4/Co_xSe_y$ composite were examined by XPS measurements. The survey scan spectra in Fig. S2† first attest the presence of all the key elements Zn, Co, Se, O, and C from the references and the composite. Fig. 3a shows the high-resolution XPS spectra of the Co 2p electrons from $ZnCo_2O_4/Co_xSe_y$. The two major peaks can be deconvoluted into two pairs of subpeaks, where the peaks with binding energy at 778.1 eV and 795.1 eV can be assigned to the Co(III) species, and the peaks with binding energy at 780.6 eV and 796.7 eV are attributable to Co(II), along with two neighboring satellite peaks at 783.9 eV and 802.4 eV.[40,52] Furthermore, as previous investigations have revealed that the co-existence of Co(II) and Co(III) can somehow lower the binding energy of the adsorption intermediates (such as O*, OH*, and OOH*) on the catalyst surface, therefore decreasing the activation energy barrier.[53] The core-level XPS spectra of the Se 3d electrons is illustrated in Fig. 3b. The broad Se 3d peak can be split into two peaks at 54.9 eV and 54.0 eV, which are assigned to the Se $3d_{3/2}$ and Se $3d_{5/2}$ electrons, respectively.[52] To further understand the synergistic catalytic effects, the chemical shift changes in the XPS spectra are analyzed. As shown in Fig. S3,† compared with Co_xSe_y, the binding energy of the Co 2p electrons decreased while the binding energy of the Se 3d electrons increased, indicating there is electron transfer occurring between Co and Se.[54,55] In addition, there is a small increase of the Co ratio once $ZnCo_2O_4$ was integrated with Co_xSe_y. Note that both Co(III) and Co(II) species are present in Co_xSe_y; however, upon the integration of $ZnCo_2O_4$ with Co_xSe_y, the Co(III) ratio significantly enhanced. As mentioned above, both Co(III) and Co(II) species are catalytically active sites for the OER, while Co(III) is more
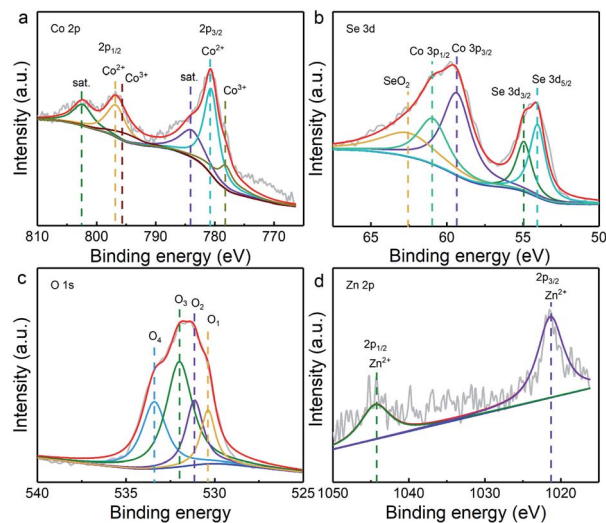

Fig. 3 High-resolution XPS spectra of the as-prepared $ZnCo_2O_4/Co_xSe_y$ sample for the (a) Co 2p, (b) Se 3d, (c) O 1s, and (d) Zn 2p electrons. Grey lines correspond to the XPS data and red lines are the fitted curves.

beneficial for facilitating the OER kinetics,[56,57] and hence the integration of $ZnCo_2O_4$ and Co_xSe_y can boost the OER performance. As shown in Fig. 3c, four oxygen contributions (530.4 eV, 531.1 eV, 532.0 eV, and 533.4 eV) can be observed upon the deconvolution of the oxygen spectra, and such four peaks are associated with the metal–oxygen bond, the oxygen in the hydroxyl group, the defect site with low oxygen coordination of small dimensions in the material, and the possible physically adsorbed water.[58,59] The high-resolution XPS spectra of the Zn 2p electrons are presented in Fig. 3d, and the fitted peaks with binding energy at 1021.4 eV and 1044.4 eV can be attributed to the Zn $2p_{1/2}$ and Zn $2p_{3/2}$ electrons from Zn(II), indicating that only Zn(II) species are present in the composite.[60] In addition, Fig. S4† presents the core-level XPS spectra of the Zn 2p, Co 2p, and O 1s electrons of $ZnCo_2O_4$, where Zn exists as Zn(II), Co is present as Co(III) and Co(II), and four oxygen contributions can be observed as well. The high-level XPS spectra of the Co 2p electrons and Se 3d electrons can also be found in Fig. S5,† where similar patterns as in the composite of $ZnCo_2O_4/Co_xSe_y$ were acquired.

The electrocatalytic performance of the as-prepared $ZnCo_2O_4/Co_xSe_y$ composite toward the OER was then evaluated in 1 M KOH solution using a typical three-electrode system. For comparison, $ZnCo_2O_4$, Co_xSe_y, and the commercial IrO_2 catalyst were also assessed under the same conditions. Fig. 4a shows the typical polarization curves for the four samples acquired at the scan rate of 10 mV s^{-1} and 1600 rpm rotation rate. It can be clearly noted that $ZnCo_2O_4/Co_xSe_y$, Co_xSe_y, and IrO_2 possessed higher OER activity than $ZnCo_2O_4$. In addition, a small peak can be observed at ~1.2 V (vs. RHE), and such an anodic peak is probably caused by the electro-oxidation process from Co^{2+} to Co^{3+} due to oxygen evolution. It can generate CoOOH species, where the Co^{3+} species can be further oxidized into Co^{4+} before the onset potential of the OER.[61,62] The
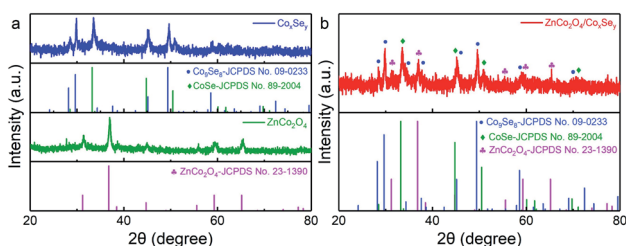

Fig. 2 The XRD patterns of (a) Co_xSe_y, $ZnCo_2O_4$, and (b) $Co_xSe_y/ZnCo_2O_4$.

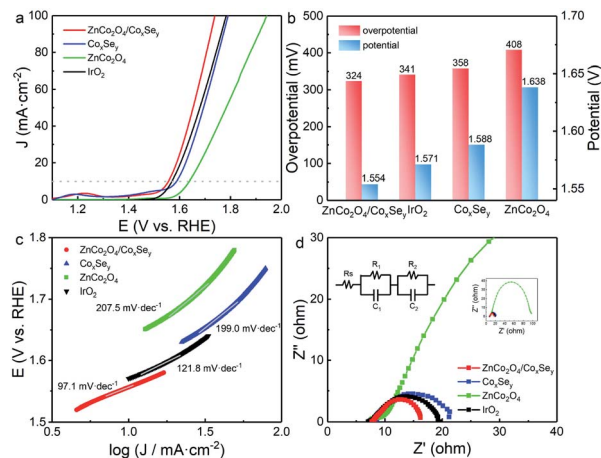**Fig. 4** (a) The OER polarization curves of Co_xSe_y, $ZnCo_2O_4$, IrO_2, and $ZnCo_2O_4/Co_xSe_y$ in 1 M KOH solution, (b) corresponding potentials and overpotentials at 10 mA cm^{-2}, (c) Tafel plots, (d) Nyquist plots of electrochemical impedance spectra (EIS) at an overpotential of 343 mV (vs. RHE) for the OER conducted in 1 M KOH aqueous solution in the high frequency range. The inset in (d) shows the Nyquist plots from the frequency range of 100 kHz to 0.01 Hz and the electronic circuit for fitting the Nyquist plots.

potentials and overpotentials at a current density of 10 mA cm^{-2} are summarized in Fig. 4b. To export a current density of 10 mA cm^{-2}, $ZnCo_2O_4/Co_xSe_y$ requires an overpotential of 324 mV, much smaller than that of Co_xSe_y and $ZnCo_2O_4$, also slightly superior to the benchmark IrO_2 catalyst.

The OER kinetics of the four catalysts were further examined by Tafel plots, as shown in Fig. 4c. The Tafel slope of $ZnCo_2O_4/Co_xSe_y$ can be calculated to be 97.1 mV dec^{-1}, much lower than that of Co_xSe_y, $ZnCo_2O_4$, and even IrO_2 (121.8 mV dec^{-1}). This suggests that $ZnCo_2O_4/Co_xSe_y$ has faster reaction kinetics. In addition, the close Tafel slope value of $ZnCo_2O_4/Co_xSe_y$ with IrO_2 suggests that the two catalysts might adopt the same OER reaction pathway and share the same rate determining step.[63–65] The Nyquist plots of Co_xSe_y, $ZnCo_2O_4$, $ZnCo_2O_4/Co_xSe_y$, and IrO_2 at 1.57 V vs. RHE are illustrated in Fig. 4d. It can be noted that the impedance response is dominated by the intermediate frequency relaxation. The impedance data are also fitted using the equivalent circuit in the inset of Fig. 4d, while the fitted values are summarized in Table S1†. It is worth pointing out that two randles-type equivalent circuit models were employed for fitting,[66] where the first one can be attributed to the ionic migration phenomenon with the electrode pores and the second one is the descriptor of the OER charge transfer at the

electrode.[26] $ZnCo_2O_4/Co_xSe_y$ had a smaller R_t $(R_1 + R_2)$ value than both $ZnCo_2O_4$ and Co_xSe_y, indicating that it possessed a more favorable charge transfer kinetics, which explains well the markedly superior OER properties.

Moreover, the cyclic voltammetric tests with various scan rates along with the double layer capacitance measurements for $ZnCo_2O_4$, Co_xSe_y, and $ZnCo_2O_4/Co_xSe_y$ were conducted, as shown in Fig. S6.† Based on the cyclic voltammograms, the electrochemically active surface area (EASA) values of the samples (Table 1) can be estimated. To accurately determine the mass contents of the elements, inductively coupled plasma atomic emission spectroscopy (ICP-AES) was performed, and the results are summarized in Table S2†. Subsequently, the turnover frequency (TOF) and mass activity (MA) were calculated (Table 1). Apparently, the $ZnCo_2O_4/Co_xSe_y$ had much higher C_{dl}, EASA, TOF, and MA values than $ZnCo_2O_4$ and Co_xSe_y, as a reflection of the structural advantages.

Note that the OER performance of the $ZnCo_2O_4/Co_xSe_y$ composite is at least comparable with, if not superior to, the recently reported Co-based nanostructured catalysts, and the comparison results are compiled in Table S3†. Such an outstanding OER performance of $ZnCo_2O_4/Co_xSe_y$ is mainly attributed to its unique structure. First of all, the $ZnCo_2O_4$ submicro/nanospheres can provide a high density of active sites for the OER on the surface;[46] secondly, Co_xSe_y nanosheets with high surface area can fully expose the OER active sites, and their hybridization with $ZnCo_2O_4$ endows the composite with enhanced conductivity;[44] finally and most importantly, through the integration of the two individual components, synergistic catalytic effects can be achieved to boost the OER performance.[63]

The long-term stability is another important criterion to evaluate the electrocatalyst for practical applications. The chronopotentiometric curves of $ZnCo_2O_4/Co_xSe_y$ and IrO_2 are illustrated in Fig. 5a. After continuous operation for 40,000 s, the current attenuated to 71.1% of its initial value for IrO_2 (28.9% loss), whereas the attenuation loss was only 1.8% for $ZnCo_2O_4/Co_xSe_y$, indicating strikingly superior long-term durability to that of IrO_2. Fig. 5b shows a multi-current-step chronopotentiometric curve for $ZnCo_2O_4/Co_xSe_y$ in 1 M KOH with the current density increasing stepwise from 20 to 200 mA cm^{-2}. It can be noted that in the beginning, the potential immediately leveled off at 1.59 V, and it remained constant in the next 500 s, and all the following steps demonstrated a similar pattern. This suggests that $ZnCo_2O_4/Co_xSe_y$ possessed a good mechanical robustness, electric conductivity, and excellent mass transport capability. The long-term durability of

Table 1 Electrochemical parameters including C_{dl}, EASA, TOF, and MA values of the as-prepared catalysts

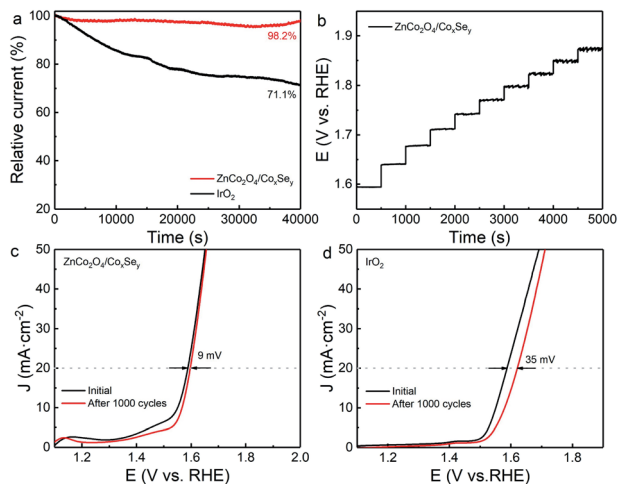| Sample	C_{dl} (mF cm^{-2})	EASA (cm^2)	TOF ($\times 10^{-3}$ s^{-1}) at η = 350 mV	MA (A g^{-1}) at η = 350 mV
$ZnCo_2O_4/Co_xSe_y$	4.3	21.07	7.10	16.76
Co_xSe_y	3.2	15.68	3.18	8.44
$ZnCo_2O_4$	3.3	16.17	0.383	1.89

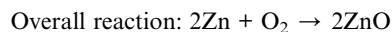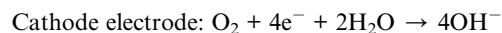**Fig. 5** (a) Chronoamperometric response (i–t) for $ZnCo_2O_4/Co_xSe_y$ at a potential of 1.57 V, (b) multistep chronopotentiometric curve of the as-prepared $ZnCo_2O_4/Co_xSe_y$ at varying current densities without iR-correction from 20 mA cm^{-2} to 200 mA cm^{-2}, with an increment of 20 mA cm^{-2} for every 500 s in 1 M KOH (c), and (d) polarization curves of $ZnCo_2O_4/Co_xSe_y$ and IrO_2 initially and after 1000 cycles in 1.0 M KOH solution.

the $ZnCo_2O_4/Co_xSe_y$ composite was further assessed and compared with IrO_2 by LSV polarization measurement before and after 1000 cycles. As shown in Fig. 5c, to achieve a current density of 20 mA cm^{-2}, only additional 9 mV overpotential was required for $ZnCo_2O_4/Co_xSe_y$ after 1000 cycles, much lower than that of IrO_2 (35 mV, Fig. 5d). The above results deliver a clear message that $ZnCo_2O_4/Co_xSe_y$ had an intriguingly superior long-term stability compared to IrO_2 for the electrocatalytic OER in alkaline media.

Besides the OER, the catalytic performance toward the ORR for the as-prepared catalysts was also tested in O_2-saturated 0.1 M KOH solution at a rotation speed of 1600 rpm. As shown in Fig. S7a,† the LSV polarization curves reveal that $ZnCo_2O_4/Co_xSe_y$ had an onset potential of 0.94 V, more positive than that of $ZnCo_2O_4$ and Co_xSe_y, approaching that of Pt/C (0.97 V). It also possessed a much larger diffusion-limited current density (4.9 mA cm^{-2}) than $ZnCo_2O_4$ and Co_xSe_y, slightly inferior to Pt/C (5.2 mA cm^{-2}). Furthermore, Tafel plots were fitted through the LSV curves to elucidate the ORR kinetics. As shown in Fig. S7b,† $ZnCo_2O_4/Co_xSe_y$ showed a Tafel slope of 79.3 mV dec^{-1}, much lower than that of $ZnCo_2O_4$ and Co_xSe_y, close to that of Pt/C (75.3 mV dec^{-1}), indicating a comparable reaction kinetics.

Encouraged by the excellent OER and ORR properties of $ZnCo_2O_4/Co_xSe_y$, its performance as the air cathode for zinc–air batteries was tested in a home-made zinc–air battery cell (see details in the Experimental section) and compared with IrO_2/C.[10,67,68] The schematic sketch for a zinc–air battery can be found in Fig. S8.† For the zinc–air battery, during the discharge process, the ORR is the functional reaction and rate-limiting step occurring at the air electrode, where the Zn plate is oxidized to ZnO and O_2 is reduced to OH$^-$.[69,70] In contrast, during the charge process, ZnO in the Zn plate is reduced to Zn(0) while the OH$^-$ is oxidized to oxygen.[69,70] Taking the

discharge process as an example, the reactions occurring at the anode and cathode in the zinc–air battery can be expressed as

$$\text{Anode electrode: } 2Zn + 4OH^- \rightarrow 2ZnO + 2H_2O + 4e^-$$

$$\text{Cathode electrode: } O_2 + 4e^- + 2H_2O \rightarrow 4OH^-$$

$$\text{Overall reaction: } 2Zn + O_2 \rightarrow 2ZnO$$

As shown in the charge–discharge polarization curves in Fig. 6a, the $ZnCo_2O_4/Co_xSe_y$ modified electrode possessed a much smaller charge–discharge voltage gap (0.98 V) than IrO_2/C (1.03 V) at a current density of 50 mA cm^{-2}, demonstrating a superior charge–discharge capability. Fig. 6b shows the discharge polarization curves and the corresponding power density. The $ZnCo_2O_4/Co_xSe_y$ electrode could gain a maximum power density of 212.9 mW cm^{-2} at 346.8 mA cm^{-2}, which is superior to that of the IrO_2/C counterpart (193.6 mW cm^{-2} at 338.4 mA cm^{-2}). As shown in Fig. S9,† the as-assembled zinc–air battery delivers an open-circuit voltage of 1.42 V for the $ZnCo_2O_4/Co_xSe_y$ air-cathode electrode, much higher than that of IrO_2/C (1.33 V). Fig. 6c shows the typical galvanostatic discharge profile of the zinc–air battery at a current density of 10 mA cm^{-2} with $ZnCo_2O_4/Co_xSe_y$ and IrO_2/C as the air cathode. The specific capacity normalized to the weight of the consumed zinc plate was determined to be 570.1 mA h g^{-1} for the
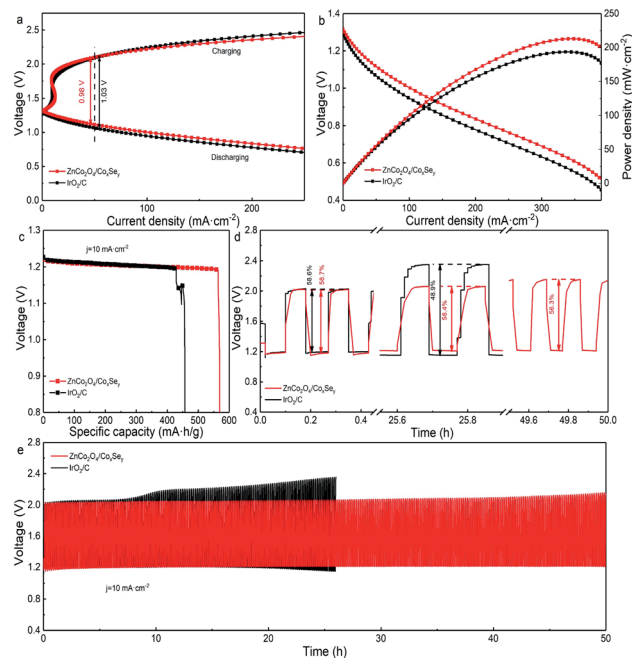

Fig. 6 (a) Charge–discharge polarization curves of zinc–air batteries using $ZnCo_2O_4/Co_xSe_y$ and IrO_2/C, (b) discharge polarization curves and power density curves of zinc–air batteries with $ZnCo_2O_4/Co_xSe_y$ and IrO_2/C, (c) specific capacities of $ZnCo_2O_4/Co_xSe_y$ and IrO_2/C at 10 mA cm^{-2}, (d) round-trip efficiency for the galvanostatic charge–discharge test at 10 mA cm^{-2}, (e) galvanostatic charge and discharge test cycling curves of zinc–air batteries using $ZnCo_2O_4/Co_xSe_y$ and IrO_2/C at 10 mA cm^{-2} with a duration of 10 min per cycle.

ZnCo$_2$O$_4$/Co$_x$Se$_y$ based battery, much higher than that of the IrO$_2$/C modified battery (457.4 mA h g^{-1}). Furthermore, as illustrated in the charge–discharge cycling test in Fig. 6d, the initial round-trip efficiency of ZnCo$_2$O$_4$/Co$_x$Se$_y$ and IrO$_2$/C was 58.7% and 58.6%, respectively. After the test for over 25 h, ZnCo$_2$O$_4$/Co$_x$Se$_y$ still maintained a high round-trip efficiency (58.4%), while the round-trip efficiency of IrO$_2$/C decreased to 48.9%. The efficiency was only reduced by ∼2.4% after operating for about 50 h, indicating the satisfactory cycling stability of ZnCo$_2$O$_4$/Co$_x$Se$_y$ as the air-cathode for zinc–air batteries. Inspired by the above performance and to further confirm the charge–discharge capacity of the ZnCo$_2$O$_4$/Co$_x$Se$_y$ based battery, the long-time stability of ZnCo$_2$O$_4$/Co$_x$Se$_y$ for the zinc–air battery was evaluated by the galvanostatic charge and discharge cycling test at a current density of 10 mA cm^{-2} with each cycle of 10 min. As presented in Fig. 6e, compared to the IrO$_2$/C air cathode, no obvious charge–discharge performance change can be observed at a current density of 10 mA cm^{-2} for ZnCo$_2$O$_4$/Co$_x$Se$_y$, even after the 50 h stability test. In addition, as summarized in Table S4,† the zinc–air battery performance of the ZnCo$_2$O$_4$/Co$_x$Se$_y$ composite is at least comparable with, if not superior to, the recently documented Co-based electrocatalysts. Finally, the morphological structure of ZnCo$_2$O$_4$/Co$_x$Se$_y$ after the charge–discharge test was probed by SEM. As shown in Fig. S10,† it exhibited no apparent change before and after the test, implying the outstanding charge–discharge stability of ZnCo$_2$O$_4$/Co$_x$Se$_y$ toward zinc–air battery applications.

Conclusions

In conclusion, the composite of 3D structure ZnCo$_2$O$_4$ submicro/nanospheres with Co$_x$Se$_y$ nanosheets has been fabricated through a facile approach. Such a composite exhibited excellent OER activity and long-term stability, superior to the benchmark IrO$_2$ catalyst. Moreover, as the air-cathode of the zinc–air battery, the composite possessed improved performance compared to the IrO$_2$/C counterpart, including a smaller voltage gap, a higher power density and specific capacity, as well as superior cycling stability along with a favorable round-trip efficiency. The excellent electrocatalytic properties of ZnCo$_2$O$_4$/Co$_x$Se$_y$ toward the OER and the zinc–air battery can be mainly attributed to the unique integrated structure between ZnCo$_2$O$_4$ submicro/nanospheres and Co$_x$Se$_y$ nanosheets, and their synergistic catalytic effects. The results here can provide an avenue to develop cost effective, efficient and durable OER electrocatalysts as alternatives for various renewable energy storage and conversion devices and beyond.

Conflicts of interest

There are no conflicts to declare.

Acknowledgements

References

1 M. G. Walter, E. L. Warren, J. R. McKone, S. W. Boettcher, Q. Mi, E. A. Santori and N. S. Lewis, *Chem. Rev.*, 2010, **110**, 6446–6473.

2 B. You and Y. Sun, *Acc. Chem. Res.*, 2018, **51**, 1571–1580.

3 Z. Xiao, Y. Wang, Y.-C. Huang, Z. Wei, C.-L. Dong, J. Ma, S. Shen, Y. Li and S. Wang, *Energy Environ. Sci.*, 2017, **10**, 2563–2569.

4 C. Zhu, Q. Shi, S. Feng, D. Du and Y. Lin, *ACS Energy Lett.*, 2018, **3**, 1713–1721.

5 K. Liang, L. Guo, K. Marcus, S. Zhang, Z. Yang, D. E. Perea, L. Zhou, Y. Du and Y. Yang, *ACS Catal.*, 2017, **7**, 8406–8412.

6 L. Shi, W. Zhou, Z. Li, S. Koul, A. Kushima and Y. Yang, *ACS Nano*, 2018, **12**, 6335–6342.

7 J. Wang, Y. Gao, D. Chen, J. Liu, Z. Zhang, Z. Shao and F. Ciucci, *ACS Catal.*, 2018, **8**, 364–371.

8 Y. Li and J. Lu, *ACS Energy Lett.*, 2017, **2**, 1370–1377.

9 D. U. Lee, P. Xu, Z. P. Cano, A. G. Kashkooli, M. G. Park and Z. Chen, *J. Mater. Chem. A*, 2016, **4**, 7107–7134.

10 K. Wang, W. Wu, Z. Tang, L. Li, S. Chen and N. M. Bedford, *ACS Appl. Mater. Interfaces*, 2019, **11**, 4983–4994.

11 X. Gu, T. Tang, X. Liu and Y. Hou, *J. Mater. Chem. A*, 2019, **7**, 11566–11583.

12 J. Yi, P. Liang, X. Liu, K. Wu, Y. Liu, Y. Wang, Y. Xia and J. Zhang, *Energy Environ. Sci.*, 2018, **11**, 3075–3095.

13 J. Fu, R. Liang, G. Liu, A. Yu, Z. Bai, L. Yang and Z. Chen, *Adv. Mater.*, 2019, **31**, 1805230.

14 D. Li, Z. Zong, Z. Tang, Z. Liu, S. Chen, Y. Tian and X. Wang, *ACS Sustainable Chem. Eng.*, 2018, **6**, 5105–5114.

15 Z. Ding, Z. Tang, L. Li, K. Wang, W. Wu, X. Chen, X. Wu and S. Chen, *Inorg. Chem. Front.*, 2018, **5**, 2425–2431.

16 Y. Li, J. Yin, L. An, M. Lu, K. Sun, Y.-Q. Zhao, D. Gao, F. Cheng and P. Xi, *Small*, 2018, **14**, 1801070.

17 Y. Jiang, Y.-P. Deng, J. Fu, D. U. Lee, R. Liang, Z. P. Cano, Y. Liu, Z. Bai, S. Hwang, L. Yang, D. Su, W. Chu and Z. Chen, *Adv. Energy Mater.*, 2018, **8**, 1702900.

18 G. Liu, J. Li, J. Fu, G. Jiang, G. Lui, D. Luo, Y.-P. Deng, J. Zhang, Z. P. Cano, A. Yu, D. Su, Z. Bai, L. Yang and Z. Chen, *Adv. Mater.*, 2019, **31**, 1806761.

19 M. S. Burke, M. G. Kast, L. Trotochaud, A. M. Smith and S. W. Boettcher, *J. Am. Chem. Soc.*, 2015, **137**, 3638–3648.

20 C. C. L. McCrory, S. Jung, J. C. Peters and T. F. Jaramillo, *J. Am. Chem. Soc.*, 2013, **135**, 16977–16987.

21 B. Wurster, D. Grumelli, D. Hötger, R. Gutzler and K. Kern, *J. Am. Chem. Soc.*, 2016, **138**, 3623–3626.

22 T. Ouyang, Y.-Q. Ye, C.-Y. Wu, K. Xiao and Z.-Q. Liu, *Angew. Chem., Int. Ed.*, 2019, **58**, 4923–4928.

23 Z.-F. Huang, J. Song, Y. Du, S. Xi, S. Dou, J. M. V. Nsanzimana, C. Wang, Z. J. Xu and X. Wang, *Nat. Energy*, 2019, **4**, 329–338.

24 D. Chen, M. Qiao, Y.-R. Lu, L. Hao, D. Liu, C.-L. Dong, Y. Li and S. Wang, *Angew. Chem., Int. Ed.*, 2018, **57**, 8691–8696.

25 H. Xu, J. Cao, C. Shan, B. Wang, P. Xi, W. Liu and Y. Tang, *Angew. Chem., Int. Ed.*, 2018, **57**, 8654–8658.

26 A. Papaderakis, N. Pliatsikas, C. Prochaska, G. Vourlias, P. Patsalas, D. Tsiplakides, S. Balomenou and S. Sotiropoulos, *J. Phys. Chem. C*, 2016, **120**, 19995–20005.

27 R. R. Rao, M. J. Kolb, N. B. Halck, A. F. Pedersen, A. Mehta, H. You, K. A. Stoerzinger, Z. Feng, H. A. Hansen, H. Zhou, L. Giordano, J. Rossmeisl, T. Vegge, I. Chorkendorff, I. E. L. Stephens and S.-H. Yang, *Energy Environ. Sci.*, 2017, **10**, 2626–2637.

28 T. Reier, M. Oezaslan and P. Strasser, *ACS Catal.*, 2012, **2**, 1765–1772.

29 L. C. Seitz, C. F. Dickens, K. Nishio, Y. Hikita, J. Montoya, A. Doyle, C. Kirk, A. Vojvodic, H. Y. Hwang, J. K. Norskov and T. F. Jaramillo, *Science*, 2016, **353**, 1011–1014.

30 Z. W. Seh, J. Kibsgaard, C. F. Dickens, I. Chorkendorff, J. K. Nørskov and T. F. Jaramillo, *Science*, 2017, **355**, eaad4998.

31 A. Ullman, Y. Liu, M. Huynh, D. K. Bediako, H. Wang, B. L. Anderson, D. C. Powers, J. J. Breen, H. D. Abruña and D. G. Nocera, *J. Am. Chem. Soc.*, 2014, **136**, 17681–17688.

32 S. L. Candelaria, N. M. Bedford, T. J. Woehl, N. S. Rentz, A. R. Showalter, S. Pylypenko, B. A. Bunker, S. Lee, B. Reinhart, Y. Ren, S. P. Ertem, E. B. Coughlin, N. A. Sather, J. L. Horan, A. M. Herring and L. F. Greenlee, *ACS Catal.*, 2017, **7**, 365–379.

33 Z. Li, W. Niu, L. Zhou and Y. Yang, *ACS Energy Lett.*, 2018, **3**, 892–898.

34 J. Wang and F. Ciucci, *Small*, 2017, **13**, 1604103.

35 D. Chen, C. Chen, Z. M. Baiyee, Z. Shao and F. Ciucci, *Chem. Rev.*, 2015, **115**, 9869–9921.

36 C. P. Plaisance and R. A. van Santen, *J. Am. Chem. Soc.*, 2015, **137**, 14660–14672.

37 S. Sun, Y. Sun, Y. Zhou, S. Xi, X. Ren, B. Huang, H. Liao, L. P. Wang, Y. Du and Z. J. Xu, *Angew. Chem., Int. Ed.*, 2019, **58**, 6042–6047.

38 T. Zhang, J. Du, P. Xi and C. Xu, *ACS Appl. Mater. Interfaces*, 2017, **9**, 362–370.

39 N. Wang, L. Li, D. Zhao, X. Kang, Z. Tang and S. Chen, *Small*, 2017, **13**, 1701025.

40 Z. Qian, Y. Chen, Z. Tang, Z. Liu, X. Wang, Y. Tian and W. Gao, *Nano-Micro Lett.*, 2019, **11**, 28.

41 P. W. Menezes, A. Indra, I. Zaharieva, C. Walter, S. Loos, S. Hoffmann, R. Schlögl, H. Dau and M. Driess, *Energy Environ. Sci.*, 2019, **12**, 988–999.

42 J. Wang, W. Cui, Q. Liu, Z. Xing, A. M. Asiri and X. Sun, *Adv. Mater.*, 2016, **28**, 215–230.

43 C. Xia, Q. Jiang, C. Zhao, M. N. Hedhili and H. N. Alshareef, *Adv. Mater.*, 2016, **28**, 77–85.

44 Y. Liu, H. Cheng, M. Lyu, S. Fan, Q. Liu, W. Zhang, Y. Zhi, C. Wang, C. Xiao, S. Wei, B. Ye and Y. Xie, *J. Am. Chem. Soc.*, 2014, **136**, 15670–15675.

45 W. Li, X. Gao, D. Xiong, F. Wei, W.-G. Song, J. Xu and L. Liu, *Adv. Energy Mater.*, 2017, **7**, 1602579.

46 Z.-Q. Liu, H. Cheng, N. Li, T. Y. Ma and Y.-Z. Su, *Adv. Mater.*, 2016, **28**, 3777–3784.

47 L. Zhuang, L. Ge, Y. Yang, M. Li, Y. Jia, X. Yao and Z. Zhu, *Adv. Mater.*, 2017, **29**, 1606793.

48 X. Wu, M. Zeng, L. Wang and J. Li, *J. Alloys Compd.*, 2019, **780**, 897–906.

49 J. Li, D. Yan, T. Lu, Y. Yao and L. Pan, *Chem. Eng. J.*, 2017, **325**, 14–24.

50 X. Zhang, J. Zhang, J. Zhao, B. Pan, M. Kong, J. Chen and Y. Xie, *J. Am. Chem. Soc.*, 2012, **134**, 11908–11911.

51 J. Deng, X. Yu, X. Qin, D. Zhou, L. Zhang, H. Duan, F. Kang, B. Li and G. Wang, *Adv. Energy Mater.*, 2019, **9**, 1803612.

52 Z. Jin, G. Zhao and Z.-S. Wang, *J. Mater. Chem. C*, 2018, **6**, 3901–3909.

53 H. Jin, J. Wang, D. Su, Z. Wei, Z. Pang and Y. Wang, *J. Am. Chem. Soc.*, 2015, **137**, 2688–2694.

54 C. Zhu, Z. Yin, W. Lai, Y. Sun, L. Liu, X. Zhang, Y. Chen and S. L. Chou, *Adv. Energy Mater.*, 2018, **8**, 1802327.

55 X. Zhang, J. Xu, H. Yuan, S. Zhang, Q. Ouyang, C. Zhu, X. Zhang and Y. Chen, *ACS Appl. Mater. Interfaces*, 2019, **11**, 39100–39108.

56 S. Palmas, F. Ferrara, A. Vacca, M. Mascia and A. Polcaro, *Electrochim. Acta*, 2007, **53**, 400–406.

57 R. Wei, M. Fang, G. Dong, C. Lan, L. Shu, H. Zhang, X. Bu and J. C. Ho, *ACS Appl. Mater. Interfaces*, 2018, **10**, 7079–7086.

58 L. An, L. Huang, P. Zhou, J. Yin, H. Liu and P. Xi, *Adv. Funct. Mater.*, 2015, **25**, 6814–6822.

59 Y. Li, C. Yang, F. Zheng, Q. Pan, Y. Liu, G. Wang, T. Liu, J. Hu and M. Liu, *Nano Energy*, 2019, **59**, 582–590.

60 J. Bai, X. Li, G. Liu, Y. Qian and S. Xiong, *Adv. Funct. Mater.*, 2014, **24**, 3012–3020.

61 X. Liu, Z. Chang, L. Luo, T. Xu, X. Lei, J. Liu and X. Sun, *Chem. Mater.*, 2014, **26**, 1889–1895.

62 Z. Zhao, H. Wu, H. He, X. Xu and Y. Jin, *Adv. Funct. Mater.*, 2014, **24**, 4698–4705.

63 T. Li, Y. Lv, J. Su, Y. Wang, Q. Yang, Y. Zhang, J. Zhou, L. Xu, D. Sun and Y. Tang, *Adv. Sci.*, 2017, **4**, 1700226.

64 Y. Wang, C. Xie, Z. Zhang, D. Liu, R. Chen and S. Wang, *Adv. Funct. Mater.*, 2018, **28**, 1703363.

65 L. An, Z. Zhang, J. Feng, F. Lv, Y. Li, R. Wang, M. Lu, R. B. Gupta, P. Xi and S. Zhang, *J. Am. Chem. Soc.*, 2018, **140**, 17624–17631.

66 W. Wu, Y. Wu, D. Zheng, K. Wang and Z. Tang, *Electrochim. Acta*, 2019, **320**, 134568.

67 I. S. Amiinu, Z. Pu, X. Liu, K. A. Owusu, H. G. R. Monestel, F. O. Boakye, H. Zhang and S. Mu, *Adv. Funct. Mater.*, 2017, **27**, 1702300.

68 T. Wang, Z. Kou, S. Mu, J. Liu, D. He, I. S. Amiinu, W. Meng, K. Zhou, Z. Luo, S. Chaemchuen and F. Verpoort, *Adv. Funct. Mater.*, 2018, **28**, 1705048.

69 J. Pan, Y. Y. Xu, H. Yang, Z. Dong, H. Liu and B. Y. Xia, *Adv. Sci.*, 2018, **5**, 1700691.

70 L. Liu, Y. Wang, F. Yan, C. Zhu, B. Geng, Y. Chen and S. l. Chou, *Small Methods*, 2020, **4**, 1900571.